Peer-Reviewed Technical Communication

Automatic Seagrass Disturbance Pattern Identification on Sonar Images

Maryam Rahnemoonfar, Abdullah F. Rahman, Richard J. Kline, and Austin Greene

***Abstract*—Natural and anthropogenic disturbances are causing degradation and loss of seagrass cover, often in the form of bare patches (potholes) and propeller-scaring from vessels. Degradation of seagrass habitat has increased significantly in recent years with losses totaling some 110 km^2 per year. With seagrass habitat disappearing at historically unprecedented rates, development of new tools for mapping these disturbances is critical to understanding habitat distribution and seagrass abundance. Current methods for mapping seagrass coverage rely on appropriate meteorological conditions (satellite imagery), are high in cost (aerial photography), or lack resolution (*in situ* point surveys). All of these methods require low turbidity, and none is capable of automatically detecting bare patches (potholes) in seagrass habitat. Sonar-based methods for mapping seagrass can function in high turbidity, and are not affected by meteorological conditions. Here, we present an automatic method for detecting and quantifying potholes in sidescan sonar images collected in a very shallow, highly disturbed seagrass bed. Acoustic studies of shallow seagrass beds ($<$2 m) are scarce due to traditional approaches being limited by reduced horizontal swath in these depth ranges. The main challenges associated with these sidescan sonar images are random ambient noise and uneven backscatter intensity across the image. Our method combines adaptive histogram equalization and top-hat mathematical morphology transformation to remove image noises and irregularities. Then, boundaries of potholes are detected using optimum binarization as well as closing and erosion mathematical morphology filters. This method was applied to several sonar images taken from the Lower Laguna Madre in Texas at less than 2-m depth. Experimental results in comparison with ground-truthing demonstrated the effectiveness method by identifying potholes with 97% accuracy.**

***Index Terms*—Image analysis, image segmentation, morphological operations, sea floor, sonar.**

I. Introduction

EXTENSIVE degradation of seagrass beds is taking place in coastal areas around the globe because of natural and human-induced disturbances. These negative impacts affect approximately 65% of the original seagrass communities, mainly in Europe, North America, and Australia [1]. While large seagrass meadows can be observed from satellite imagery and aerial methods these approaches can be limited by high turbidity, poor meteorological conditions, or low resolution. Mapping of seagrass degradation due to natural and human disturbances such as potholes and propeller scars is essential to estimating overall abundance, disturbance regimes, and the overall health of related marine systems. Since the early 1990s, various remote sensing techniques have been exploited for seagrass mapping [2]–[9] and all have their limitations. For both aerial and satellite optical remote sensing techniques, it is difficult to detect seagrass disturbances under water. For optical remote sensing, light is attenuated as it passes through the water column and reflects back from the benthos causing errors in calculations. The attenuation is not only the function of depth of the water column but also the sediment load, microalgae and organic matters in the water column. As water depth increases, increased attenuation makes optical imagery even more difficult to capture. Furthermore, shallow coastal waters can be turbid due to wind and wave action, boat traffic, coastal constructions, and other human activities—all of which create limitations in seagrass and disturbance mapping effectiveness using optical sensors. Methods typically used to categorize and map terrestrial vegetation based on spectral reflectance of vegetation such as normalized difference vegetation index do not function well in seagrass habitats due to the reflective and refractive properties of the water column above the seagrass. These conditions limit most seagrass imagery to simple visual analysis, where the effects of disturbance cannot be accurately quantified. Only the visible bands of multispectral satellite sensors are generally used to map seagrass occurrence and boundaries in coastal shallow waters.

Underwater acoustic techniques have allowed many advances in the field of remote sensing and these techniques can be used to produce a high-definition, 2-D sonar image of seagrass ecosystems [10]. However, several studies have shown the inefficiency of operating traditional acoustic instruments such as sidescan or multibeam sonar in shallow conditions [11]–[15]. Recent work by Greene [16] has extended operational sidescan surveys of seagrass ecosystems into shallow seagrass beds at depths of 2 m or less. Shallow habitats such as these have remained largely understudied in acoustic surveys of submerged aquatic vegetation. However, these advancements are largely due to a reduction in transducer beam angle and as such traditional techniques to normalize backscatter-intensity [such as time variable gain (TVG)] demonstrate limited effectiveness. The acoustic profile of this benthic ecosystem is created when sound waves are emitted, reflected back, and received by the transducer of a sonar device. The intensity and contours of the image are determined by the position and amount of time a sound wave takes to return to the transducer. In this paper, we use sonar imagery as a tool to recognize disturbance patterns in seagrass beds. Previous literature regarding sonar image pattern recognition has mainly focused on searching for solid objects on a sandy sea floor [17]–[24]. A Markovian segmentation algorithm was used by Mignotte *et al*. [17] to segment the sonar image. Additionally, they used an unsupervised hierarchical Markov random field model [18] to segment the image into two kinds of regions: 1) shadow and 2) sea-bottom reverberation. Even though they obtained good results for simple concrete objects with regular shape on a sandy sea floor, their particular method would be complicated and computationally expensive to apply on seagrass images with irregular and complex patterns. Furthermore,

Manuscript received October 3, 2016; revised May 12, 2017 and September 7, 2017; accepted December 1, 2017. A short and early version of this paper was previously published in Proc. SPIE, vol. 9844, Automatic Target Recognition XXVI, 98440C, May 12, 2016; doi: 10.1117/12.2224191. *(Corresponding author: Maryam Rahnemoonfar.)*

Associate Editor: J. Cobb.

M. Rahnemoonfar is with the Computer Vision and Remote Sensing Laboratory, School of Engineering and Computing Sciences, Texas A&M University-Corpus Christi, Corpus Christi, TX 78412 USA (e-mail: maryam.rahnemoonfar@tamucc.edu).

A. F. Rahman, R. J. Kline, and A. Greene are with the Coastal Studies Laboratory, School of Earth, Environmental, and Marine Sciences, University of Texas Rio Grande Valley, Brownsville, TX 78520 USA (e-mail: abdullah.rahman@utrgv.edu; richard.kline@utrgv.edu; AustinLG@Hawaii.edu.

Digital Object Identifier 10.1109/JOE.2017.2780707

another sonar segmentation method was described by Lianantonakis *et al*. [19]. Their particular method focused on the binary segmentation of high-resolution sonar images. The first step was to extract texture features from a sidescan image containing two distinct regions. Then, a region based active contour model was applied to the vector valued images extracted from the original data. An automatic image analysis program for the detection and identification of stationary targets, such as meter-sized concrete artificial reefs on the sea floor was proposed by Tian *et al*. [20]. In this algorithm, features were extracted using grey level cooccurrence matrix and then classified by a Bayesian classifier. Another sonar image segmentation method was created by Ye *et al*. [21]. Their method first involved the extraction of local texture features of sonar images based on Gauss–Markov random field model and integrated into the level-set energy functions. Even though the sidescan sonar has been used for benthic mapping, there is no prevailing method that automatically detects the extent of seagrass beds or automatically identifies and maps its disturbance. To the best of our knowledge, this research is the first of its kind on automated seagrass disturbance identification using sidescan sonar imagery. Sonar images are notorious for having random ambient noise and low signal-to-noise ratio, which makes the segmentation of targets, such as seagrass, difficult to accomplish. Additionally, brightness levels throughout the image can be nonuniform, potentially making segmentation of natural and man-made disturbances within seagrass difficult. Moreover, disturbance presents complex patterns in images causing most segmentation techniques to fail. We collected sonar images in Lower Laguna Madre of South Texas, which contains vast seagrass beds situated behind a barrier island. To detect disturbances in seagrass structure, we describe here, a novel technique based on mathematical morphology and adaptive histogram equalization for recognition of potholes within shallow seagrass structure in sidescan sonar images.

The following are the contributions of this work.

1) A novel approach for automated seagrass disturbance identification is presented.
2) Our method is robust to noise, uneven backscatter intensity, and complex seagrass pothole patterns.
3) Seagrass and pothole map are generated automatically for the first time.
4) Testing and development of sidescan sonar for shallow water.

II. Methodology

Our approach consisted of two major steps, as shown in Fig. 1. In the first step, we performed uneven backscatter intensity reduction, and the image was enhanced based on adaptive histogram equalization, top-hat transformation, and Gaussian adaptive thresholding. In the second step, we identified seagrass blowouts (or potholes, a disturbance regime) by applying, Otsu binarization, closing, and erosion morphological operators [25], [26].

A. Image Enhancement

While capturing the data, the sidescan sonar transmits a high-frequency acoustic signal in the water using two parallel transducers. There were substantial variations in brightness found in the sidescan sonar images because the objects closer to the transducer created brighter reflections. Fig. 2 shows a sonar image in which the brightness values vary across the image. In the central portion of the image, there is a higher intensity of reflection, which makes the image look brighter; whereas in both sides of the image the reflection is of lower intensity and the image looks darker. The bright line in the middle of the image is the first echo return of the sonar at the seafloor underneath the boat.

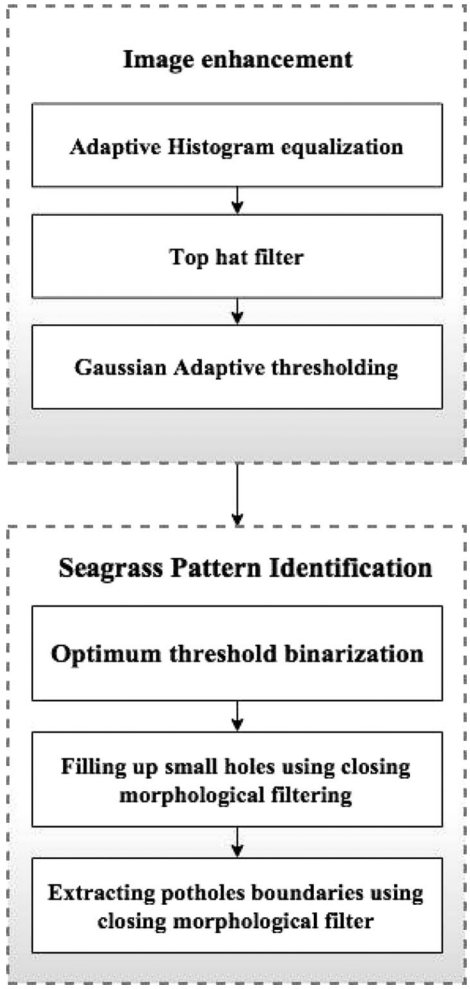

Fig. 1. Flowchart of overall methodology.

Potholes are visible on the image, scattered irregularly and shown as depressions in the seagrass bed.

Uneven backscatter intensity at this shallow recording depth and very low grazing angle creates a real challenge for automatic detection of potholes in seagrass. Normalization of the images could not be accomplished with commonly used methods such as TVG or beam angle correction. Here, we explain that how we mitigated this issue. From Fig. 2, it is clear that there are mainly three partitions that include a bright partition in the middle and two relatively dark partitions in the sides. We performed horizontal line by line scan from both directions. The idea was to find two locations (b_1 and b_2) within the line to divide it into three different sections, namely two darker portions on the sides and one bright portion in the middle. Locations b_1 and b_2 were selected such that the bright portion is between b_1 and b_2. We used histogram interpretation to select the threshold value (T) that we used for each line to select b_1 and b_2. In Fig. 3, we plotted a histogram of the highlighted subset, where the expected break point lies. The peak of the histogram in Fig. 3 was 0.4, so a threshold (T) of 0.4 was set to identify the breakpoints b_1 and b_2 for each line.

The boundaries between darker and brighter partition is defined as a set, B, of all the break points. Mathematically, B can be expressed as

$$B = \{(b_1, b_2, i) | 0 \leq i < n, b_1 = F_1(i, T), b_2 = F_2(i, T)\} \quad (1)$$

where n is the number of horizontal pixel lines in the image, T is a predefined threshold parameter, and F_1 and F_2 are the functions returning the length of the first run of pixels in $i\text{th}$ line whose intensity

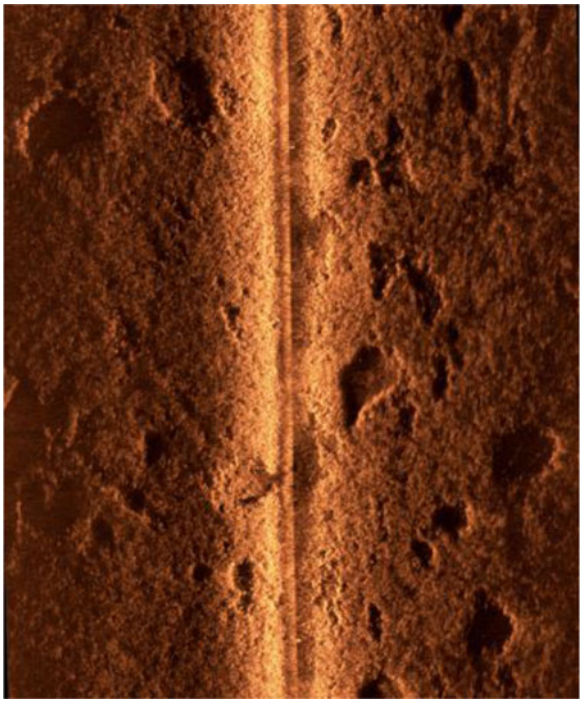

Fig. 2. Example of a sidescan sonar image with uneven backscatter intensity across the image.

value is greater or equal to T. F_1 returns the length starting from first pixel while scanning in the forward direction and F_2 returns the length starting from the last pixel while scanning in a backward direction. We then applied an adaptive histogram equalization separately on each partition for adjusting image intensities to enhance contrast. Each row of the image was partitioned into three sections using partition points b_1 and b_2, as described in (1). The histogram equalization [27] is an effective image enhancing technique, summarized as follows: Let $\mathbf{X} = \{X(i,j)\}$ be an image where $\{X(i,j)\}$ denote gray value at location (i,j). If the total number of pixels is N, and image intensity is digitized to L, levels are then $\forall X(i,j) \in \{X_0, X_1, \ldots, X_{L-1}\}$. Suppose n_k is the total number of pixels with gray value X_k then, the probability density of the X_k will be

$$p(X_k) = n_k / N, \qquad k = 0, 1, \ldots, L-1 \tag{2}$$

and its cumulative distribution function can be defined as

$$c(X_k) = \sum_{i=0}^{k} p(X_k), \qquad k = 0, 1, \ldots, L-1. \tag{3}$$

The transformation function can be defined as

$$f(X_k) = X_0 + (X_{L-1} - X_0)c(X_k), \qquad k = 0, 1, \ldots, L-1. \tag{4}$$

If $\mathbf{Y} = \{Y(i,j)\}$ is defined as an equalized image, then

$$\mathbf{Y} = f(\mathbf{X}) = \{f(X(i,j))|\forall X(i,j) \in \mathbf{X}\}. \tag{5}$$

After applying the adaptive histogram equalization, we used a Top-hat mathematical morphology filter to further remove the uneven backscatter intensity defects in the image. top-hat filtering computes the morphological opening of the image and then subtracts the result from the original image. It uses the structuring element. Top-hat transformation is defined as the function minus its opening [26]

$$T_{\mathrm{hat}}(f) = f - (f \circ b) \tag{6}$$

where f is the original image, b is the structure element, and $\circ$ is the opening morphological operator. Opening of *A* by *B* is the erosion of *A* by *B* followed by dilation of the result by *B* [28]. With *A* and *B* as sets in Z^2, the erosion of *A* by *B*, denoted by $A \ominus B$ is defined as

$$A \ominus B = \{z|(B)_z \cap A^c = \emptyset\} \tag{7}$$

and the dilation of A by B can be defined as

$$A \oplus B = \{z|(\hat{B})_z \cap A \neq \emptyset\}. \tag{8}$$

Structure elements are small sets or subimages used to probe an image under study. Here, the structure element used was a circle with a radius of 15 pixels. The goal of top-hat transformation is to extract the uniform background image. Therefore, all objects including potholes must be removed during the erosion stage of top-hat. Since the maximum size of a pothole is around 130 cm by 130 cm and the resolution of image is around 10 cm per pixel, a structure element of size 15 pixels will remove all objects and only give us the background image.

To further enhance the image, we applied the Gaussian adaptive thresholding technique. In this method, a variable threshold was calculated at every point, (*x*,*y*) based on the properties computed in a neighborhood of (*x*,*y*). In Gaussian adaptive thresholding, the threshold value is a weighted sum of the small neighborhood around each pixel. The neighborhood windows were chosen small enough so that the backscatter intensity of each is approximately uniform. A threshold is calculated for each pixel based on the convolution of the image with Gaussian function as follows [26]:

$$T(x,y) = \sum_{k}^{a} \sum_{l=-b}^{b} G(s,t) f(x-k, y-l) \tag{9}$$

where G is the Gaussian function of two variables and has the basic form of

$$G(x,y) = \frac{1}{2\pi\sigma^2} e^{-\frac{x^2+y^2}{2\sigma^2}} \tag{10}$$

where σ is the standard deviation.

B. Seagrass Pattern Identification

After enhancing the image and removing the effect of nonuniform backscatter intensity, the process of extracting potholes from the sonar images was conducted. The image was binarized using an optimum Otsu threshold [29]. If the threshold to binarize the image is *t*, then optimal threshold can be defined as maximum of $\sigma_B^2(t)$ as follows:

$$\sigma_B^2(t^*) = \max_{0 \le t \le L-1} \{\sigma_B^2(t)\} \tag{11}$$

where $\sigma_B^2(t)$ is class variance and L is total number of gray levels in the image. $\sigma_B^2(t)$ can be defined as follows:

$$\sigma_B^2(t) = \omega_0(t)[\mu_0(t) - \mu_T]^2 + \omega_1(t)[\mu_1(t) - \mu_T]^2 \tag{12}$$

where $\mu_T = \sum_{i=0}^{L-1} iP_i$, $\omega_0(t) = \sum_{i=0}^{l} P_i$, $\omega_1(t) = 1 - \omega_0(t)$, $\mu(t) = \sum_{i=0}^{l} iP_i$, $\mu_0(t) = (\mu(t))/(\omega_0(t))$, $\mu_1(t) = (\mu_T - \mu(t))/(1-\omega_0(t))$, $P_i = (n_i)/(N)$, $N = \sum_{i=0}^{L-1} n_i$, and n_i is the number of pixels with gray level i.

After binarization, there were a lot of small holes remaining which were, in fact, part of seagrass texture. To eliminate these small holes, we applied a closing morphological filter. If *A* is the image and *B* is structure element, then the Closing of *A* by *B* can be defined as the dilation of *A* by *B* followed by erosion of the result of the dilation

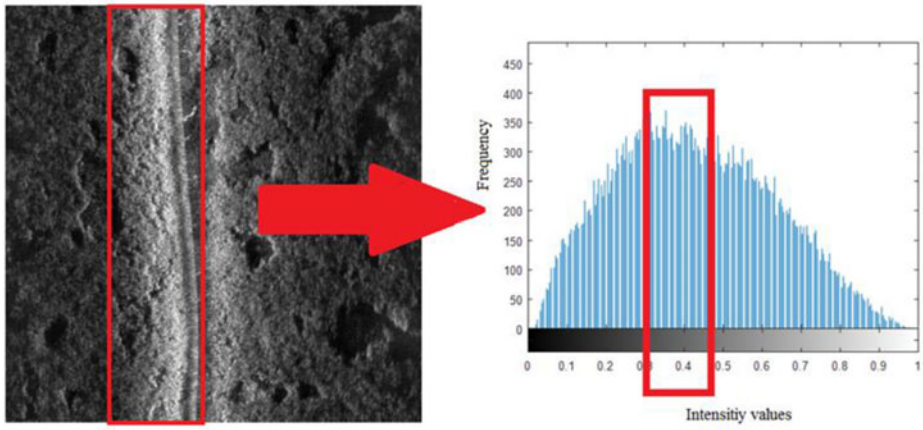

Fig. 3. Histogram of the highlighted subset of the seagrass image.

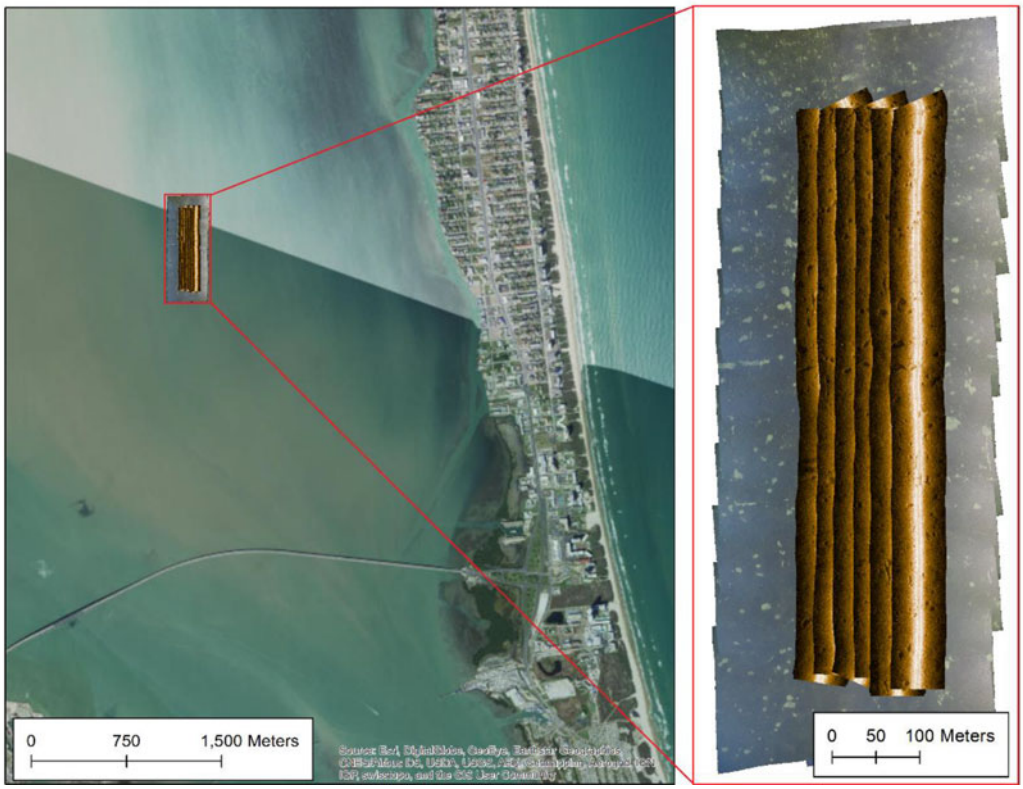

Fig. 4. Location of the study site with the six sonar transects.

by B [26]

$$A \odot B = (A \oplus B) \ominus B. \tag{13}$$

For our analysis, we used a circle as the structural element with diameter of 11 pixels since we were interested in detecting pothole with a diameter greater than 11 pixels. The closing operation smoothed out sections of contours by eliminating small holes and filling gaps in the contour. Subsequently, the boundary of objects in the image was calculated using the following formula [26]:

$$\beta\ (A) = A - (A \ominus B) \tag{14}$$

where A is the original image and $\ominus$ is the erosion mathematical morphology operator.

III. Experimental Results

A. Data Description

Data were collected from the seagrass beds of the Lower Laguna Madre in Southern Texas on May 23, 2016 from an average depth of 75 cm. A specialized sidescan sonar unit was constructed consisting of a towfish with two Lowrance Structure Scan HD LSS-2 transducers, a dual-beam 200-kHz down-imaging transducer connected to a Humminbird 998C HD SI control unit [30]. The sidescan unit was operated at 800 kHz, and the transducers were offset at 25° from the horizontal to allow improved horizontal swath in shallow environments [16]. Vessel position was measured with a heading-sensor equipped GPS receiver mounted directly over the transducer. Water depth was measured via the 200-kHz down-imaging transducer. All navigation and

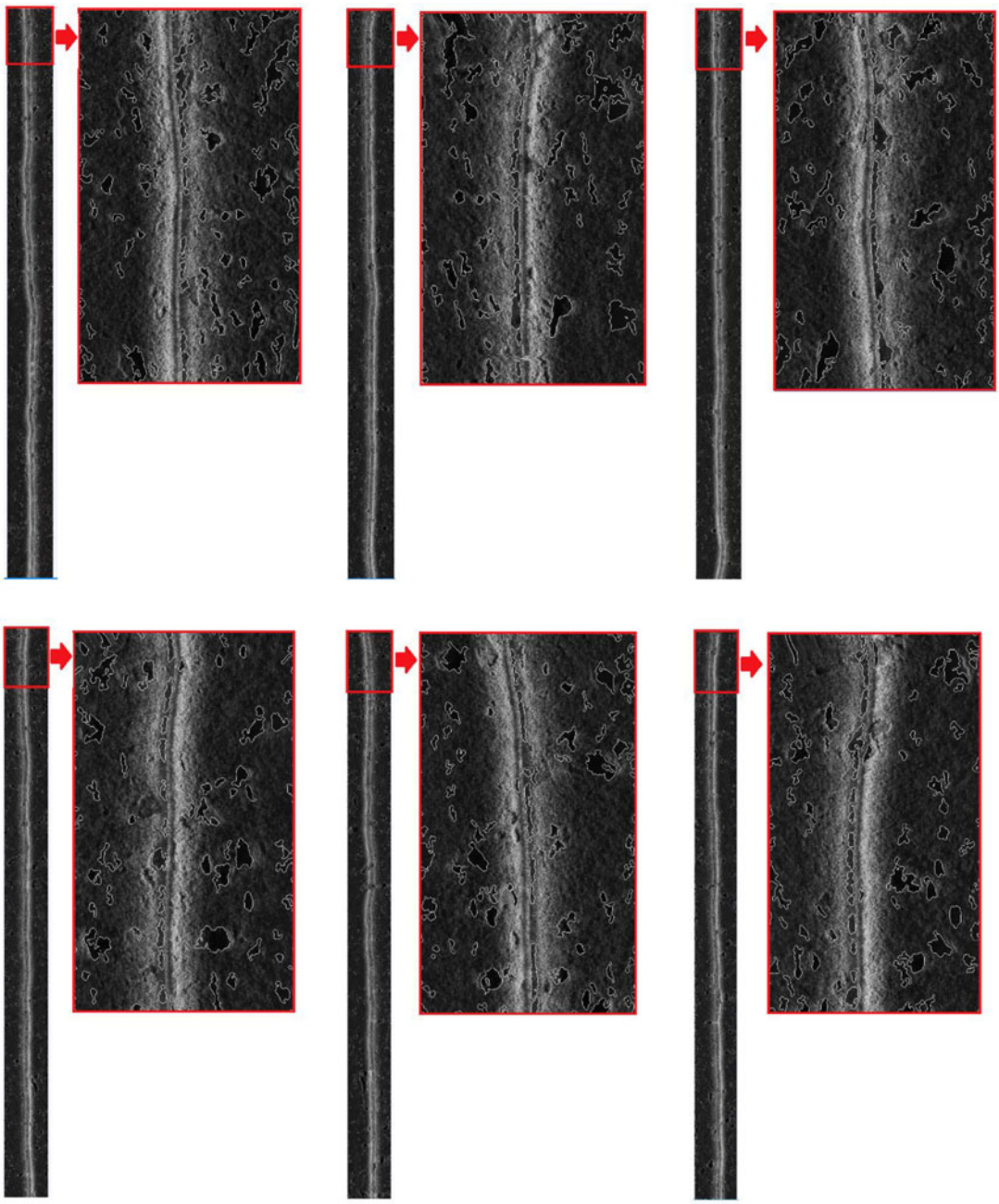

Fig. 5. Transect images with a zoomed subset of final result.

acoustic signals were recorded continuously by the Humminbird 998C HD SI control unit on a secure digital (SD) card for later processing. Combining each line of reflected signal with its position, time, and depth produced an image of the seafloor (see Fig. 2). A total of six transects approximately $5000 \times 60\,000$ pixels and overlapping by 50% were processed individually to image an area of approximately 88 000 m^2. Fig. 4 shows the location of the study site on GeoEye imagery with the six transects of sonar images used in this experiment.

B. Seagrass Pattern Recognition

The images used in this experiment were large transects. Each transect was 600 m long, and spaced 20 m apart with a horizontal swath of approximately 50 m. Total area covered between all six transects was 88 000 m^2 $(150\ m \times 600\ m)$. We applied the seagrass detection algorithm on entire transect images, however, for a better display, only a subset is shown here. Fig. 5 shows the original transect images along with the subset chosen for display and part of the result superimposed on the subset.

Fig. 6 shows the original image and all the intermediate results while identifying the potholes along with the ground-truth. We present here, a subset of one of the six transect images.

The uneven, nonlinear backscatter intensity gradients are likely the product of either the modified sidescan array's reduced beam pattern, sound attenuation by seagrass aerenchym, the very shallow environment in which the sidescan was designed to operate, or a combination of these. These factors did not permit backscatter-intensity normalization with a TVG without a heavy loss in detail along the center track. However, automatic gain correction (AGC) appeared to approximate

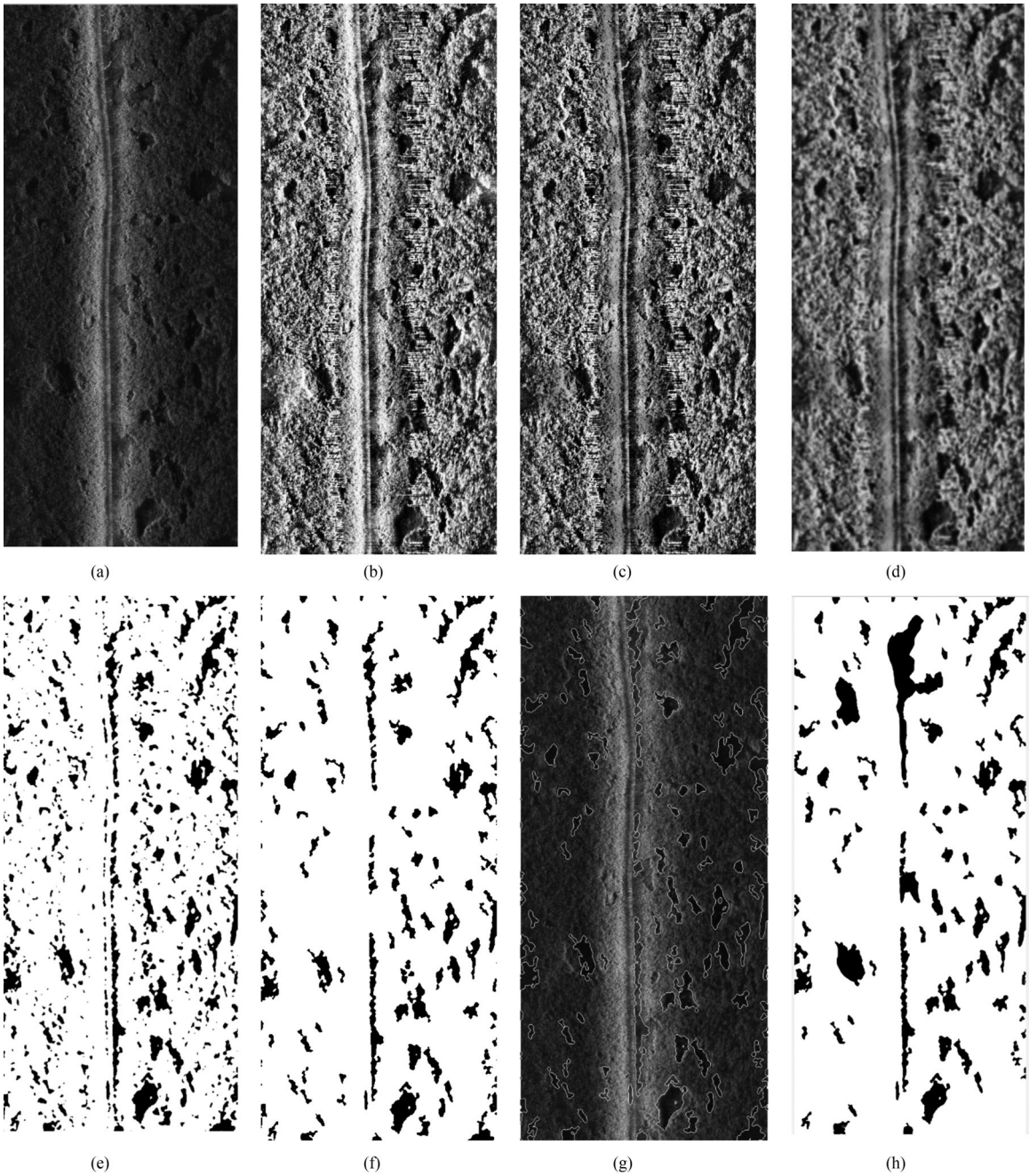

Fig. 6. (a) Subset of the original image. (b) Result after applying histogram equalization. (c) Result after applying the top-hat filter. (d) Result after applying the Gaussian smoothing filter. (e) Result after applying binarization. (f) Result after removing small holes from the binary image. (g) Image obtained after superimposing the boundaries of the potholes over the original image. (h) Ground-truth.

our own adaptive gain equalization. A traditional sidescan array operating over deeper seagrass meadows may be able to simplify image processing and pattern recognition steps by utilizing these automated techniques such as TVG correction. Fig. 6(a) represents the subset of the original image. In Fig. 6(b), it can be observed that after applying adaptive histogram equalization (5), the darker sides of the original image were brighter but still the middle section of the image was still brighter, as compared to sides. To mitigate this effect, we applied Top-hat filter (6) on the image in Fig. 6(b) and (c). This filter was effective at balancing the backscatter intensity. The image is too sharp to be binarized at this point of time because of the seagrass texture. Due to the extreme sharpness of the seagrass texture in the image, a Gaussian filter was used before binarization to prevent artifacts being identified as potholes that were only the texture of the seagrass. After applying Gaussian filter (9) with $\sigma = 2$, a smoother image was observed in Fig. 6(d) with reduced sharpness of the seagrass texture. After binarizing of the image (11), we can see many small potholes in Fig. 6(e). A closing morphological filter (13) was applied, revealing the actual potholes in Fig. 6(f). Finally, the boundaries of potholes were detected using (14). The final polygons were superimposed on the original image, shown in Fig. 6(g). Fig. 6(h) shows the ground-truth image. This image was obtained by manual inspection of the image and annotation by an expert with detailed experience in the seagrass area that was imaged.

TABLE I
EXAMPLE OF AN ERROR MATRIX

		i = column (reference)			Row total
		1	2	k	n_{i+}
j = row (classification)	1	n_{11}	n_{12}	n_{1k}	n_{1+}
	2	n_{21}	n_{22}	n_{2k}	n_{2+}
	k	n_{k1}	n_{k2}	n_{kk}	n_{k+}
Column total	n_{+j}	n_{+1}	n_{+2}	n_{+k}	n

TABLE II
OVERALL AND CLASSWISE ACCURACY ASSESSMENT

Average overall naïve accuracy (%)		97.73
Average overall kappa accuracy (%)		85.96
Average producer's kappa Accuracy	Potholes	83.33
	Seagrass	88.84
Average user's kappa Accuracy	Potholes	89.00
	Seagrass	83.03

TABLE III
OVERALL AND CLASSWISE ERROR ASSESSMENT

Average overall kappa error (10^{-5})		5.58
Average producer's kappa Accuracy	Potholes	7.83
	Seagrass	6.76
Average user's kappa Accuracy	Potholes	7.84
	Seagrass	6.76

C. Performance Evaluation and Accuracy Metrics

Visual interpretation of the results suggests that the algorithm was able to detect potholes efficiently and an accuracy assessment confirms this same result in Table II. We used several matrices for the accuracy assessment including Naïve and kappa accuracy measures of both, overall and classwise comparisons. naïve overall accuracy was computed as follows [31]:

$$\text{naïve overall accuracy} = \frac{\sum_{i=1}^{k} n_{ii}}{n}. \tag{15}$$

Assuming that n samples are distributed into k^2 cells, where each sample is assigned to one of k categories in the remotely sensed classification (rows) and, independently, to one of the same k categories in the reference data set (columns). As shown in Table I, let n_{ij} denote the number of samples classified into category i $(i = 1, 2, \ldots, k)$ in the remotely sensed classification and category j $(j = 1, 2, \ldots, k)$ in the reference data set (ground-truth).

Generally, naïve accuracy measure is used, but in this case, it is not a reliable measure because it does not take into account the random agreement for two classes. Since we had only two classes (seagrass and potholes), there was a 50% chance for a pixel to belong to any one of the classes, we used kappa statistics [15] to compute both overall and classwise accuracies.

The kappa index of agreement (KIA) reveals how much better, or worse, the classifier is than would be expected by random chance. The overall kappa index is defined as follows [31]:

$$\kappa = \frac{\theta_1 - \theta_2}{1 - \theta_2} \tag{16}$$

where κ is kappa, $\theta_1 = (1/n)\sum_{i=1}^{k} n_{ii}$ and $\theta_2 = (1/n^2)$ $\sum_{i=1}^{k} n_{i+}n_{+i}$, n_{+i} is Marginal sum of column i and n_{i+} Marginal sum of row i

$$\text{kappa user's accuracy} = \frac{nn_{ii} - n_{i+}n_{+i}}{nn_{i+} - n_{i+}n_{+i}} \tag{17}$$

$$\text{kappa producer's accuracy} = \frac{nn_{jj} - n_{+j}n_{j+}}{nn_{+j} - n_{+j}n_{j+}}. \tag{18}$$

We computed the average of all the six images for both the overall naïve and classwise kappa accuracies. The average overall naïve accuracy was 97.73%. Despite the high overall naïve accuracy, we also computed kappa accuracies because naïve accuracy is not free from random agreement and may not be a reliable measure for two classes. For classwise accuracies, we computed both producer's and user's accuracy. Producer's accuracy, also known as precision, corresponds to error of omission (exclusion). It accounts for the samples, which are not classified in a class that they actually belong to, while user's accuracy, also known as recall, presents the reliability of classes in the classified image. Along with the accuracies, we also computed the standard error of each computed accuracy. Tables II and III show that the pothole detection accuracies are high and errors are very low (on the order of 10^{-5}) and that potholes have more user's accuracy as compared to seagrass. Pothole identification was more reliable as compared to seagrass identification. However, some of the potholes could not be identified correctly and classified as seagrass, leading to a lower producer's accuracy. The average overall and classwise accuracies and errors are presented in Tables II and III. Figs. 7 and 8 show accuracies and error, respectively, for all the six images. It can be observed from Fig. 7 that the overall kappa for six images ranged from 82% to 90% accuracy with an average kappa accuracy of 85.96%.

Figs. 9–11 show some subset of the seagrass images, where big, intermediate, and small size potholes were accurately identified.

In this study, potholes were identified with the high accuracy regardless of their size (see Figs. 9–11). Moreover, our algorithm was able to detect potholes in any portion of the seagrass image despite the uneven backscatter intensity in the sonar image. In Fig. 11(a) and (b), potholes are in the brighter portion of the seagrass image (middle of the image) and all other subsets from Figs. 9–11 potholes are in darker portion of the image.

There were few false negative and false positives in our pothole identifications; however, some false positives occur when there is similar texture inside and outside of potholes. In Fig. 12, it can be observed that the pothole boundary is not identified accurately. Moreover, a close observation of the Fig. 12 reveals that the area within the pothole, which was not detected as pothole (highlighted by upper red box), has a similar texture to that of seagrass (highlighted by lower red box). Two possible reasons for the texture similarity are: 1) presence of macroalgae inside the pothole or 2) due to the new growth of seagrass inside the pothole. Algae within the potholes may reflect sonar signals similar to the sea-

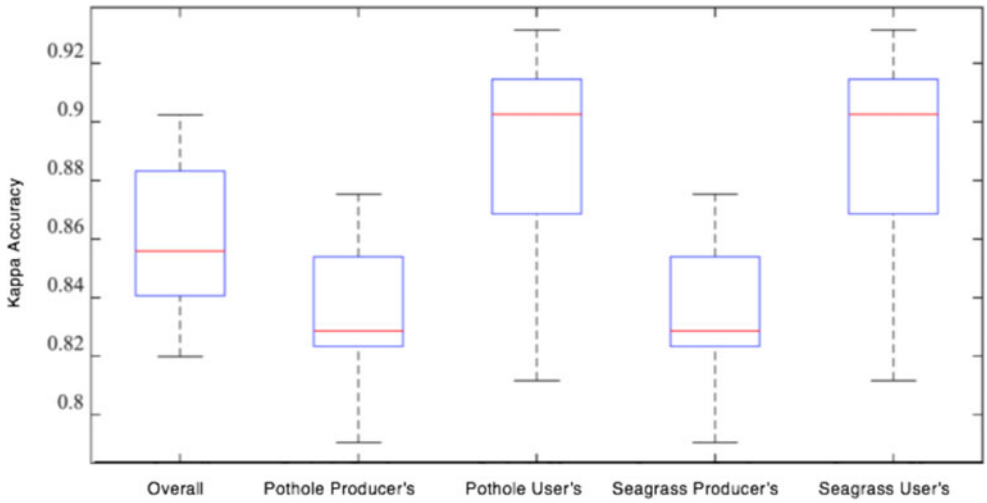

Fig. 7. Overall and classwise kappa accuracies for six transect images.

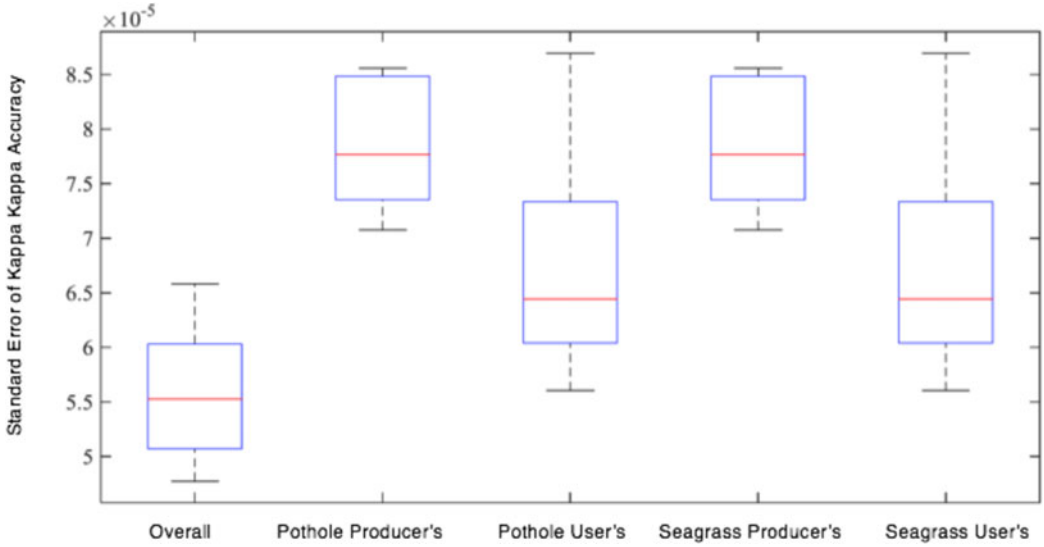

Fig. 8. Overall and classwise standard error of kappa for six transect images.

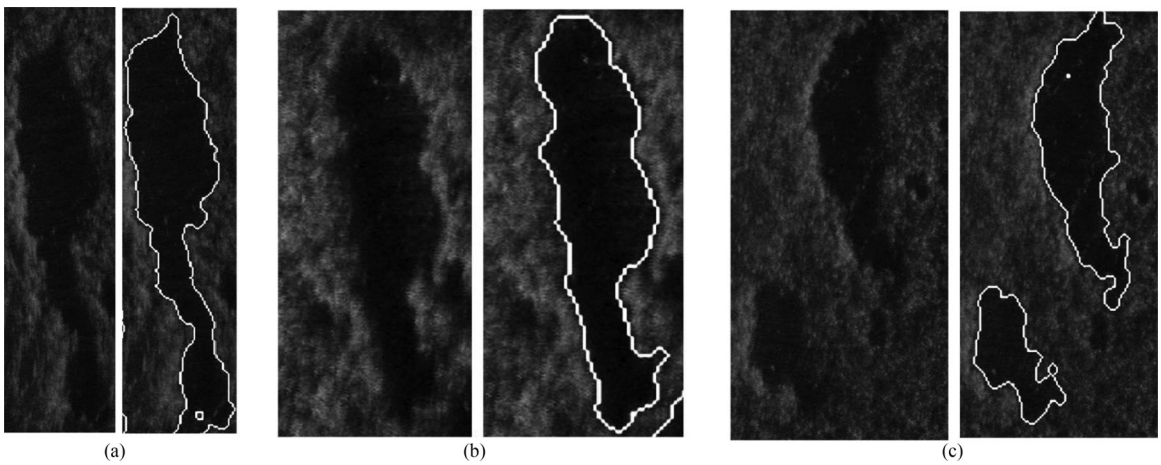

Fig. 9. Accurately identified big size potholes over different seagrass images (left: original image; right: detected polygons with our proposed method).

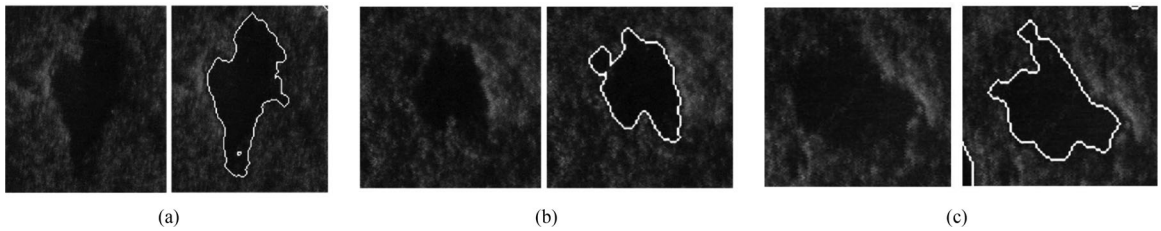

Fig. 10. Accurately identified intermediate size potholes over different seagrass images.

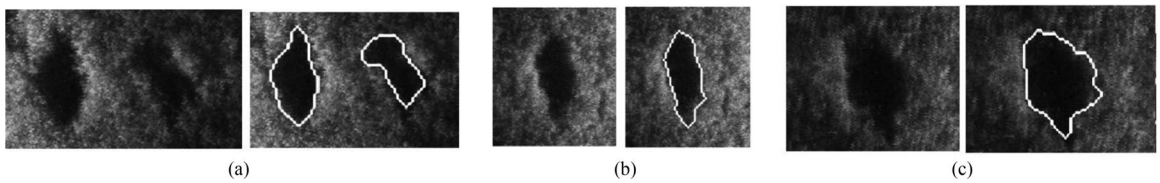

Fig. 11. Accurately identified small size potholes over different seagrass images.

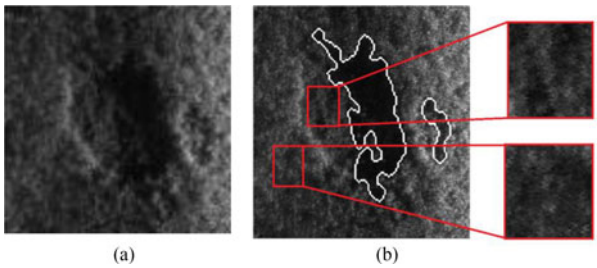

Fig. 12. (a) Subset of the original image having a large pothole and (b) subset of the image containing boundaries of the potholes identified by the algorithm along with the zoomed subsets of the areas within the pothole and outside the pothole.

grass, leading to misidentification of potholes as seagrass as seen in Figs. 7 and 8 in terms of user's and producer's accuracy and errors.

Another problem in disturbance identification was with boat propeller scars. Currently, the algorithm presented here is not able to detect propeller scars accurately. Since the scars are very narrow linear features, they dissolve with the seagrass while smoothing the image and are left unidentified. Future research will investigate separate narrow linear feature detection based algorithms to identify the propeller scars.

IV. Conclusion

In this study, we demonstrated an automated method to detect seagrass potholes using sidescan sonar imagery from a modified sidescan array functioning in a shallow environment. Presence of uneven backscatter intensity and noise in sidescan sonar images, in addition to the complex pothole patterns, created several challenges in recognizing seagrass disturbance pattern in the sonar images. We approached these challenges in two steps, namely, 1) image enhancement and 2) seagrass pattern recognition. For image enhancement, our automated method combined adaptive histogram equalization and top-hat mathematical transform to remove image noises and irregularities. Commonly used sonar gain normalization methods such as TVG or AGC may accomplish similar results as adaptive histogram equalization when operating in deeper conditions via traditional sidescan arrays. Surveying a shallow and highly disturbed seagrass meadow, we designed a wholly automatic technique to detect the boundary of seagrass bed potholes using mathematical morphology filters. We applied our algorithm to sidescan sonar images collected from Lower Laguna Madre in Texas and experimental results in comparison with the ground-truthing show the high accuracy (∼97%) of the proposed technique in detecting the potholes. Paired with a sidescan array modified for use in very shallow depths, these results demonstrate an efficient and accurate method of automatically identifying disturbance in shallow seagrass meadows rarely attempted using acoustic instruments. In the future, we plan to extend this work to real-time identification of seagrass disturbance patterns.

References

[1] H. K. Lotze *et al.*, "Depletion, degradation, and recovery potential of estuaries and coastal seas," *Science*, vol. 312, pp. 1806–1809, 2006.

[2] M. Hossain, J. Bujang, M. Zakaria, and M. Hashim, "Assessment of landsat 7 scan line corrector-off data gap-filling methods for seagrass distribution mapping," *Int. J. Remote Sens.*, vol. 36, pp. 1188–1215, 2015.

[3] A. G. Dekker, V. E. Brando, and J. M. Anstee, "Retrospective seagrass change detection in a shallow coastal tidal Australian lake," *Remote Sens. Environ.*, vol. 97, pp. 415–433, 2005.

[4] H. Dierssen, A. Chlus, and B. Russell, "Hyperspectral discrimination of floating mats of seagrass wrack and the macroalgae sargassum in coastal waters of greater Florida Bay using airborne remote sensing," *Remote Sens. Environ.*, vol. 167, pp. 247–258, 2015.

[5] V. Pasqualini *et al.*, "Use of SPOT 5 for mapping seagrasses: An application to Posidonia Oceanica," *Remote Sens. Environ.*, vol. 94, pp. 39–45, 2005.

[6] S. Phinn, C. Roelfsema, A. Dekker, V. Brando, and J. Anstee, "Mapping seagrass species, cover and biomass in shallow waters: An assessment of satellite multi-spectral and airborne hyper-spectral imaging systems in moreton bay (Australia)," *Remote Sens. Environ.*, vol. 112, pp. 3413–3425, 2008.

[7] C. M. Roelfsema *et al.*, "Multi-temporal mapping of seagrass cover, species and biomass: A semi-automated object based image analysis approach," *Remote Sens. Environ.*, vol. 150, pp. 172–187, 2014.

[8] C. C. Wabnitz, S. Andréfouët, D. Torres-Pulliza, F. E. Müller-Karger, and P. A. Kramer, "Regional-scale seagrass habitat mapping in the Wider Caribbean region using landsat sensors: Applications to conservation and ecology," *Remote Sens. Environ.*, vol. 112, pp. 3455–3467, 2008.

[9] J. Hedley, B. Russell, K. Randolph, and H. Dierssen, "A physics-based method for the remote sensing of seagrasses," *Remote Sens. Environ.*, vol. 174, pp. 134–147, 2016.

[10] M. Hossain, J. S. Bujang, M. Zakaria, and M. Hashim, "The application of remote sensing to seagrass ecosystems: an overview and future research prospects," *Int. J. Remote Sens.*, vol. 36, pp. 61–114, 2015.

[11] B. M. Sabol, R. E. Melton, R. Chamberlain, P. Doering, and K. Haunert, "Evaluation of a digital echo sounder system for detection of submersed aquatic vegetation," *Estuaries Coasts*, vol. 25, pp. 133–141, 2002.

[12] T. Sagawa *et al.*, "Technical Note. Mapping seagrass beds using IKONOS satellite image and side scan sonar measurements: A Japanese case study," *Int. J. Remote Sens.*, vol. 29, pp. 281–291, 2008.

[13] M. Paul, A. Lefebvre, E. Manca, and C. L. Amos, "An acoustic method for the remote measurement of seagrass metrics," *Estuarine, Coastal Shelf Sci.*, vol. 93, pp. 68–79, 2011.

[14] A. Lefebvre, C. Thompson, K. Collins, and C. Amos, "Use of a high-resolution profiling sonar and a towed video camera to map a Zostera marina bed, Solent, UK," *Estuarine, Coastal Shelf Sci.*, vol. 82, pp. 323–334, 2009.

[15] G. De Falco, R. Tonielli, G. Di Martino, S. Innangi, S. Simeone, and I. M. Parnum, "Relationships between multibeam backscatter, sediment grain size and Posidonia Oceanica seagrass distribution," *Continental Shelf Res.*, vol. 30, pp. 1941–1950, 2010.

[16] A. Greene, "Applications of side scan and parametric echosounders for mapping shallow seagrass habitats and their associated organic carbon," M.S. thesis, Dept. Bio. Sci., School of Earth, Environ., Marine Sci., Univ. Texas Rio Grande Valley, Brownsville, TX, USA, 2017.

[17] M. Mignotte, C. Collet, P. Perez, and P. Bouthemy, "Three-class Markovian segmentation of high-resolution sonar images," *Comput. Vis. Image Understanding*, vol. 76, no. 3, pp. 191–204, 1999.

[18] M. Mignotte, C. Collet, P. Perez, and P. Bouthemy, "Sonar image segmentation using an unsupervised hierarchical MRF model," *IEEE Trans. Image Process.*, vol. 9, no. 7, pp. 1216–1231, Jul. 2000.

[19] M. Lianantonakis and Y. R. Petillot, "Sidescan sonar segmentation using active contours and level set methods," presented at the OCEANS Eur. Conf., Brest, France, 2005.

[20] W. Tian, "Automatic target detection and analyses in side-scan sonar imagery," in *Proc. WRI Global Congr. Intell. Syst.*, 2009, pp. 397–403.

[21] X.-F. Ye, Z.-H. Zhang, P. X. Liu, and H.-L. Guan, "Sonar image segmentation based on GMRF and level-set models," *Ocean Eng.*, vol. 37, pp. 891–901, 2010.

[22] J. T. Cobb, K. C. Slatton, and G. J. Dobeck, "A parametric model for characterizing seabed textures in synthetic aperture sonar images," *IEEE J. Ocean. Eng.*, vol. 35, no. 2, pp. 250–266, Apr. 2010.

[23] F. A. Sadjadi, "Studies in adaptive automated underwater sonar mine detection and classification—Part 1: Exploitation methods," *Proc. SPIE*, vol. 9476, 2015, Art. no. 94760K.

[24] J. C. Isaacs, "Laplace–Beltrami eigenfunction metrics and geodesic shape distance features for shape matching in synthetic aperture sonar," in *Proc. IEEE Comput. Soc. Conf. Comput. Vis. Pattern Recogn. Workshops*, 2011, pp. 14–20.

[25] Z. Qu and L. Zhang, "Research on image segmentation based on the improved Otsu algorithm," in *Proc. 2nd Int. Conf. Intell. Human–Mach. Syst. Cybern.*, 2010, pp. 228–231.

[26] R. C. Gonzalez and R. E. Woods, *Digital Image Processing*. Upper Saddle River, NJ, USA: Prentice-Hall, 2008.

[27] Y. Wang, Q. Chen, and B. Zhang, "Image enhancement based on equal area dualistic sub-image histogram equalization method," *IEEE Trans. Consum. Electron.*, vol. 45, no. 1, pp. 68–75, Feb. 1999.

[28] R. M. Haralick, S. R. Sternberg, and X. Zhuang, "Image analysis using mathematical morphology," *IEEE Trans. Pattern Anal. Mach, Intell.*, vol. PAMI-9, no. 4, pp. 532–550, Jul. 1987.

[29] N. Otsu, "A threshold selection method from gray-level histograms," *Automatica*, vol. 11, pp. 23–27, 1975.

[30] M. L. Quammen and C. P. Onuf, "Laguna madre: seagrass changes continue decades after salinity reduction," *Estuaries*, vol. 16, pp. 302–310, 1993.

[31] R. G. Congalton and K. Green, *Assessing the Accuracy of Remotely Sensed Data: Principles and Practices*. Boca Raton, FL, USA: CRC Press, 2008.

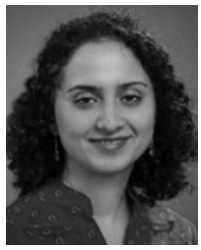

Maryam Rahnemoonfar received the Ph.D. degree in computer science from the University of Salford, Manchester, U.K., in 2010 and the M.Sc. degree in remote sensing engineering from the University of Tehran, Tehran, Iran, in 2005.

She is currently an Assistant Professor in Computer Science and the Director of the Computer Vision and Remote Sensing Laboratory (Bina lab), Texas A&M University Corpus Christi, Corpus Christi, TX, USA. Her research interests include image processing, computer vision, machine learning, remote sensing, and synthetic aperture radar.

Abdullah F. Rahman received the Ph.D. degree in hydrology and remote sensing from the University of Arizona, Tucson, AZ, USA, in 1996.

He is currently a Professor at the School of Earth, Environmental, and Marine Sciences, University of Texas Rio Grande Valley (UTRGV), Brownsville, TX, USA. He is a member of the Blue Carbon Scientific Working Group, an international group of researchers studying carbon in coastal ecosystems of seagrasses, mangroves, and tidal salt marshes. Before joining UTRGV, he was an Associate Professor at Indiana University, Bloomington, IN, USA. His expertise is on the use of remote sensing for studying carbon stocks and fluxes of ecosystems.

Richard J. Kline received the Ph.D. degree in marine science from the University of Texas at Austin, Austin, Texas, USA, in 2010 and the M.Sc. degree in fisheries and aquatic sciences from the University of Florida, Gainesville, Florida, USA, in 2004.

He is currently an Associate Professor at the School of Earth, Environmental, and Marine Sciences, University of Texas Rio Grande Valley (UTRGV), Brownsville, TX, USA. His research interests include the fields of conservation and applied ecology and physiology, especially application of new technology to address research questions in coastal and marine environments.

Austin Greene received the B.S. degree in evolution, ecology, and biodiversity from the University of California, Davis, CA, USA, in 2014 and the M.S. degree in biological sciences from the University of Texas Rio Grande Valley, Brownsville, TX, USA, in 2017. He is currently working toward the Ph.D. degree at the University of Hawaii at Manoa, Honolulu, HI, USA, studying the drivers and spatial distribution of disease on coral reefs.

His research interests include anthropogenic drivers of environmental change and the development of low-cost sensors to encourage their study.